



AMERICAN UNIVERSITY

---

W A S H I N G T O N , D C

Measuring Ocean Winds from Space  
Using a Radar Satellite

Michael Robinson

Co-Authors: Morgan Dehart, Matt Hubler,  
Mark Verdi, Zhu Zhu

November 2013

Technical Report No. 2014-1

SIX-MONTH RESEARCH REPORT

---

## Measuring ocean winds from space using a radar satellite

---

*Principal Investigator:*

Prof. Michael ROBINSON  
Assistant Professor  
226 Gray Hall  
Mathematics and Statistics  
American University  
Office: (202)885-3681  
Mobile: (484)477-3345  
michaelr@american.edu

*Research team:*

Morgan DEHART  
Matt HUBLER  
Mark VERDI  
Zhu ZHU



AMERICAN UNIVERSITY

## 1. EXECUTIVE SUMMARY

Winds influence the ocean surface in a complicated (and not well-understood) way that depends on ocean chemistry, density, and temperature. Understanding the small-scale structure of winds over the ocean surface is critical for understanding the impact of certain rapidly-evolving environmental problems, such as oil spills, algal blooms, and floating debris.

The key factor limiting our understanding of weather patterns over the ocean is low resolution wind data from outdated sensors and overly simplistic analytic methods. Current satellite-borne wind measuring systems give wind measurements spaced 2.5 km apart [18]; our approach yields similarly accurate measurements a few hundred meters apart, largely due to the availability of higher resolution data products from TerraSAR-X. Our focus is on the spatial variability of the ocean surface at small scales (tens of meters), and therefore largely addresses the visibility of *gusts*.

The project aims to (1) to acquire experimentally-controlled high-resolution ocean imagery from TerraSAR-X, and (2) to develop novel, sophisticated image processing algorithms to analyze the resulting data. Thus far, we have focused primarily on the first of these goals, and successfully processed high-resolution SAR images of the ocean surface using standard algorithms and have begun to validate them against coincident wind measurements from oceanographic buoys. The collection campaign centered on two major regions of interest: (1) where there is substantial variability in direction (Gulf of Mexico), and (2) where there is variability in speed (off the coast of Portland, OR, USA).

We exhibit several important findings:

- (1) We found that *gusts are sometimes more visible in VV-polarization images than in HH-polarized images.*
- (2) We found that skipping the usual step of converting SAR spectra to wave spectra saves computation time and *does not diminish the visibility of gusts.*
- (3) We present a *new way to display wave direction* that is better adapted to the careful study of small-scale irregularities.
- (4) We *assess the theoretical validity* of wave direction measurement from spectral subimages, rather than merely comparing it with low-resolution *in situ* buoy data.
- (5) We *completely validated a model of spectral cutoff* in the azimuthal direction.

Next steps include:

- (1) Systematic validation of SAR-derived wind and wave estimates against buoy-derived measurements,
- (2) A second collection campaign, focused on repeat-pass variability of the patch of ocean near a single buoy, and
- (3) Development of enhanced, novel algorithms based on our group's pioneering work in topological filters.

## CONTENTS

1. Executive summary	1
2. Problem statement	2
3. Historical summary	3
3.1. Existing processing approaches	3
4. Pre-collection experiment	5
5. Experimental design	6
5.1. Locations	6
5.2. Available buoys	7
5.3. Imaging modes used	8
6. Processing methodology	9
6.1. Azimuthal cutoff	10
6.2. Range spectral models	12
6.3. Visualization of spectral angles	14
6.4. Noise performance of spectral angle measurement	15
7. Data overview	17
7.1. Pixel radar cross section distribution	18
7.2. Qualitative of overview of local spectra	18
8. Detailed analysis of spectra	19
8.1. Validation of azimuthal cutoff	19
8.2. Spectral block size study	21
8.3. Analysis of 1d spectral cuts	24
8.4. Spectral spatial variability study	26
9. Analysis of LSRA filtered images	27
9.1. LSRA filtered image highlights	28
9.2. Polarization comparisons	29
9.3. LSRA window tuning study	29
10. Next steps	30
10.1. Validation	31
10.2. New data collection	32
10.3. Algorithm development	32
References	32

## 2. PROBLEM STATEMENT

The goal of this project is to develop and validate image processing algorithms for measuring wind direction over the ocean. We plan to use wind truth data from (1) oceanographic buoys and other anchored sensors and (2) wind measurements from other satellite sensors to validate our SAR-derived wind direction estimates. Both of these sources of truth data are of necessarily lower resolution than what is available from TerraSAR-X. It is worth noting that buoy validation is already routinely done against the ASCAT sensor [14]. Our collection campaign centers on several buoys described in the NOAA's database [20]. We are using the resulting concurrent data stream for validation of spectral shape, but have not completely validated the recovery of wind direction from the image.

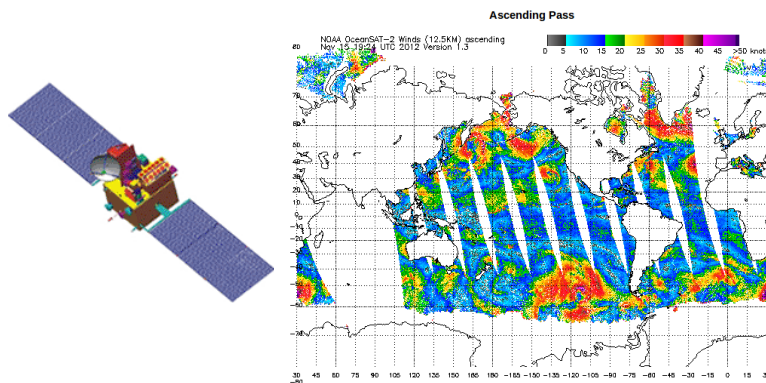


FIGURE 1. The OSCAT platform (left) and sample wind speed product (right)

### 3. HISTORICAL SUMMARY

Predictive models of the weather rely on accurate wind estimates [1]. It is well known that the predictions given by weather models are highly sensitive to errors in the input wind measurements. (One of the best-known examples of chaos, the Lorenz system, was discovered in a simplified weather model.) The errors due to low resolution measurements can significantly impact the inferences one makes from these models, especially if they are used for providing long-term climatological insight [25].

Existing remote measurement of ocean winds is usually performed using a device called a satellite-borne *scatterometer*. This device transmits a radio signal aimed at the ocean surface and measures the amount of energy reflected back to the satellite. There is a functional relationship (which has been tabulated by many previous researchers, for instance [24]) between wind speed, ocean surface roughness, and the strength of radio echoes reflected from the surface – higher wind speed results in greater reflectivity. Additionally, a higher fraction of energy is returned to the satellite when looking parallel to the wind. This idea enables satellites to measure the wind direction.

To date, ASCAT, OSCAT (Figure 1), WindSAT, SSM/I QuickSCAT, and the now-defunct ERS-2 have been flown and produce publicly-available near-real-time wind direction and speed over all major bodies of water [9].

**3.1. Existing processing approaches.** Our goal is to use high resolution SAR images to estimate the speed and direction of the wind over the ocean. Fielded scatterometer systems produce these estimates, but suffer from low spatial and temporal resolution. They provide measurements spaced kilometers apart, and additionally require two coincident collections for each measurement. Since these two collections are taken from different portions of the orbit, a given measurement incorporates two separate observations that are minutes apart (or longer). Therefore, quickly changing phenomena cannot be measured, especially if they are physically small. A gust can dissipate or move over the time interval between image acquisitions.

Because of this, we focus on the extraction of wind vectors from a single collection, so the acquisition time is about 10 seconds. This provides an opportunity to

measure quickly changing phenomena whose physical scale is smaller. At present, we have focused on spectral methods, which are well-established in the literature.

Young [27] has shown that a 3d Fourier analysis (2 space dimensions and 1 time dimension) of boat-mounted navigational radar images yields information on the surface wave field and near-surface currents. Compared to 2d analysis (2 space dimensions), which has an inherent directional ambiguity and typically a low signal to noise ratio, the 3d analysis can provide information on the wave phase speed, magnitude, and direction of near surface currents.

Spaceborne SAR is a valuable way to examine the surface of the ocean, and is being used to detect stormwater runoff plumes, municipal wastewater plumes, natural hydrocarbon seeps, surface pollution, and ship wakes. [22, 11, 5] The use of 2d local spectra to extract wave direction from spaceborne SAR images was initially pioneered by [10] using SEASAT. Hasselmann and Hasselmann [12] quantified some of the nonlinear effects induced on local spectra by motion, which lead to a spectral inversion algorithm. Extracting wave direction from spectra has good support in the literature [3, 13] and was recently applied to TerraSAR-X imagery in [4, 2] to great effect. Additionally, Collard [3] used the ENVISAT wave mode to measure the wave height and direction. They found good agreement between wave spectra derived from SAR and *in situ* measurements.

A few researchers have addressed differences between the radar polarization response of the ocean surface, for instance [16, 8]. However, a systematic analysis of polarimetry has not been done.

3.1.1. *How our approach differs.* The disadvantage of all active scatterometers is that their resolution is very limited. In particular, the finest resolution is on the order of a kilometer or so [18]. This tends to limit the time resolution of the measurements as well; it takes time for waves to develop. Scatterometry has no way to assess the age of waves, so it is unclear how rapidly the wind conditions are changing on a minute-to-minute basis. Rapidly changing winds do not result in variations in large waves, due to inertia.

This project takes a different approach, by instead imaging small groups of waves, from which the wave direction can easily be measured. This will enable us to measure not just large-scale wind phenomena through mature wave structure, but also smaller spatial scales. These smaller spatial scales will reveal wave structure over shorter *time* scales as well. The focus of this effort is on *gust detection* and the analysis of turbulence at small spatial scales.

Because of this goal, we follow a very similar algorithmic approach to [10], but differ in a number of places:

- (1) Our focus is on detecting *small-scale irregularities* (like [4]) in high resolution products (like those of [2]).
- (2) We use this technique as a tool to compare the visibility of gusts in HH- and VV-polarized images. We found that *gusts are sometimes more visible in VV-polarization images* than in HH-polarized images.
- (3) We examine the angles associated to SAR spectra directly, rather than first preprocessing them into wave spectra. While this is strictly incorrect, *skipping the preprocessing step saves computation time and does not diminish the visibility of gusts.*
- (4) We *completely validated a model of spectral cutoff* in the azimuthal direction (based on [12]).

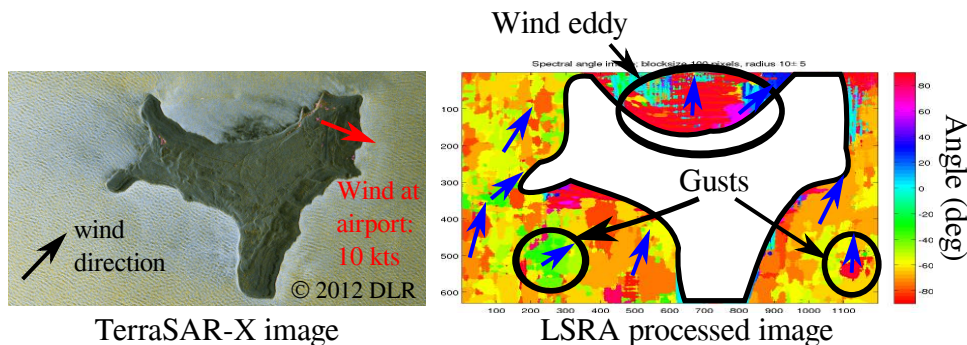


FIGURE 2. Christmas island sample imagery (left), output of our angle-sensitive filter (right)

- (5) We perform tests in simulation and on the data to *assess the theoretical validity* of the method for detecting small wind features, rather than merely comparing it with low-resolution *in situ* buoy data (which we have also begun to do, but have not completed).
- (6) We present the wave direction data as a colored image plot, rather than a quiver (field of arrows) plot. This has the advantage of presenting a *less-cluttered view of small wind features*.

#### 4. PRE-COLLECTION EXPERIMENT

Before embarking on a TerraSAR-X collection campaign, we tested our initial proposed algorithm against imagery from the TerraSAR-X website that is available to the public. This reduced program risk by giving us an opportunity to test and refine our algorithm and identify hurdles relevant to data collection before we submitted a data request.

We selected the 26 Nov 2012 image of Christmas Island [6], since waves are visible on the surface of the ocean. In particular, one can see the orientation of waves in the surface of the ocean (black arrow on left frame of Figure 2). This is *not* typical of SAR images of the ocean, since the wave structure is usually much less apparent. That the wind is blowing strongly with a relatively constant direction is also apparent, since there is a large eddy to the north of the island. Consistent with the functional relationship between wind speed and surface reflectivity, the pixel radar cross section of the ocean in the eddy is lower than to the south of the island, where the wind is faster.

To corroborate this visual assessment, we acquired the day’s wind history from the airport on Christmas Island [26]. The wind direction at the airport is shown by a red arrow on left frame of Figure 2. This wind direction is not parallel to the apparent wave direction on the surface of the ocean, which is probably a result of turbulence from the eddy. The airport’s wind direction measurement is probably not a very reliable indicator of ocean wave direction – this is why we rely on *in situ* buoys in what follows.

The right frame of Figure 2 shows the output of our algorithm after some preliminary adjustments to the minimum and maximum spectral radii described in Section 6.3.1. The eddy-related effects in the north of the island are readily seen,

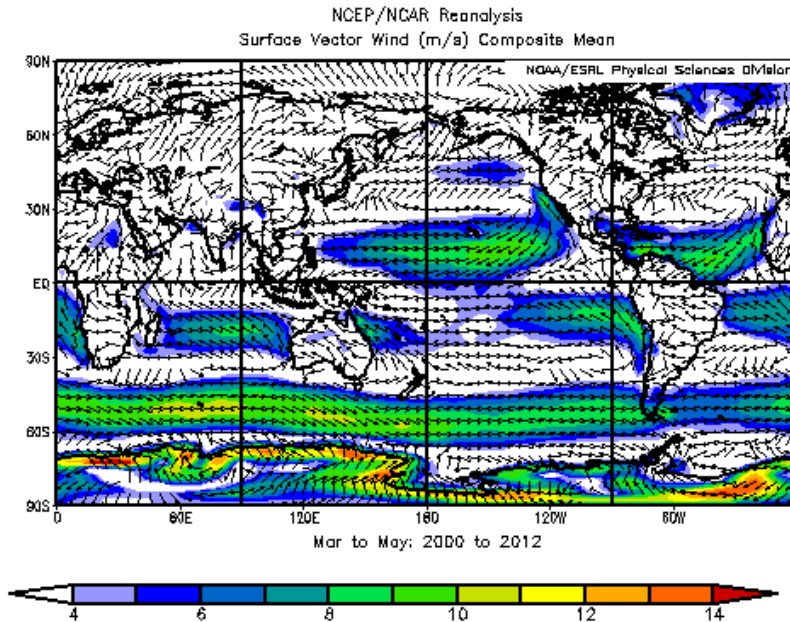


FIGURE 3. Average wind conditions worldwide for the 12 years before our collection window (March-May) [19]

as well as some “edge effects” around the coast of the island (especially to the south east). These effects are visible in the original image, but are difficult to see: the wind deflects slightly due to drag as it flows around the island. Although both of these effects can be validated by examining the original TerraSAR-X image, neither are open-ocean effects. However, two areas away from the island to the south east and south west have noticeably different wave direction. We believe these are due to the presence of local gusting or calming in those areas.

## 5. EXPERIMENTAL DESIGN

The goal of this program is to develop sophisticated image processing algorithms to extract wind speed and direction from high-resolution TerraSAR-X images of the ocean surface. In order to validate the results produced by our algorithms, we plan to compare them against coincident wind measurements from oceanographic buoys in the SAR scene. These algorithms could enable the scientific community to exploit TerraSAR-X scenes containing bodies of water to measure the wind structure near the water’s surface.

**5.1. Locations.** In order to verify that our results are accurate, we collected images near active weather buoys put in place by the US National Oceanic and Atmospheric Administration (NOAA). Since our algorithms measure both wave direction and



FIGURE 4. Locations of NOAA buoys providing wind and wave conditions in the two focus areas

TABLE 1. Buoys used for experimental collections

Name	Region	Wind	Current	Wave spectrum
NOAA 46089	Portland	Y	N	Y
NOAA 42360	Gulf	Y	Y	N

wind speed, we chose two areas of open ocean based on the historical variability of these properties (Figure 4):

- (1) An area near the center of the Gulf of Mexico, where we hoped to capture wind directional variance, and
- (2) An area off the coast of Portland, Oregon, USA, where we hoped to detect higher wind speeds.

From the study of composite historical data from NOAA [19] (see Figure 3, for instance), we can tell that the ocean wind speed and direction can be highly unstable. We have looked at two months of data and concluded that anomalously high ocean wind speed or direction happened one out of ten days in a typical location in the ocean. Historical analysis in the vicinity of the Portland aimpoint indicates that while the wind speed is variable there, the direction is typically stable over longer periods of time. Furthermore, the wind is not very turbulent in the surrounding area.

**5.2. Available buoys.** Both of the areas under analysis have a large number of buoys in place and would allow for proper verification of our results (see Figure 4). We selected buoys (Table 1) based on the historical wind conditions of the area, buoy capabilities, and buoy location.

For the Portland images, we selected the NOAA buoy 46089 as the aimpoint. Located 85 nautical miles west northwest of Tillamook, OR, 46089 provides continuous wind speed data, spectral wave density, and principal wave angle, though it does not supply current information. There are several other buoys nearby that could be used for additional validation if desired, and the proximity to the shore could allow us to validate against local weather reports as well.

In contrast to the Portland region, the Gulf of Mexico region was chosen to emphasize variability in wind direction. There are several available buoys in close proximity to each other, so we selected an area near the center of the Gulf. Therefore, we do not expect local weather reports to validate our findings. Due to the high buoy population density of the Gulf of Mexico we were able to select a buoy nearby several others (two buoys have coordinates that place them in our acquired images) and may be able to use the individual outputs from each buoy to validate our findings.

In the Gulf of Mexico image, we selected NOAA buoy 42360 as the aimpoint. Stationed over Walker Ridge, 42360 measured wind speed and direction data as well as ocean current data. Unfortunately, the lack of wave data from 42360 made it more difficult to verify certain spectral measurements taken from the Gulf images.

For future collections, we have assembled a list of buoys (Table 5) that measure the data that we need to verify our results, prioritizing wind and wave data over ocean current data collection. The prioritization comes as we can hone the precision of our models through these two measurements more than the current data. Ideally, the buoys would constitute the center of a collected image. However we believe that the images now being analyzed are sufficiently close to their respective buoy locations to verify our experimental findings, even though they are not visible in the images.

**5.3. Imaging modes used.** To gather the data essential to the research, we requested data takes labeled in the form of EEC\_SE.SM.S and EEC\_SE.SM.D. Due to the experimental aspect of analyzing the data, we wanted to discern whether single or dual polarization (that is the S and D on the designations) fulfills our research needs. Our initial analysis indicates that VV polarization is often more useful, which is only available in the dual polarization products.

We collected stripmap mode (SM) data takes since we wanted the best possible resolution over a swath. We attempted to center the data takes around an active buoy off the coast in regions of different wind patterns.

Additionally, the modes and designations selected for the data take allow for ground resolutions of  $3.5 \text{ m}^2$  pixels in single polarization and  $6.6 \text{ m}^2$  in dual polarization which gives us the accuracy to check for individual or smaller groupings of waves. Since we targeted the best resolution with our selection of the stripmap mode, we aim to maintain incidence angles as close to  $45^\circ$  as possible for all data takes.

We selected the Enhanced Ellipsoid Correction (EEC) mode since products with this designation have elevation models that correct the images taken and adjust for elevation of the terrain and the curvature of the Earth. Even though we are looking at open ocean regions, our aim of using buoys brings us closer to the coast and possibly near small rocks or islands. The EEC was chosen to not only account for the curvature inherent in the images and in order to hedge against encountering

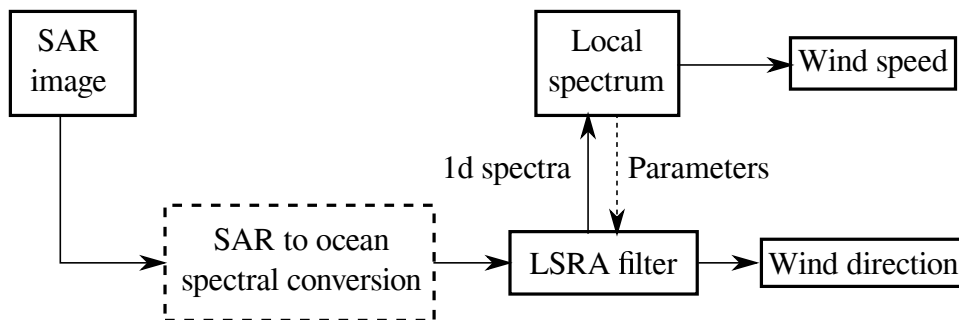


FIGURE 5. Processing methodology flowchart. At the time of writing, the spectral conversion (dotted box) is under development and is merely a pass-through.

rogue geographical features (including possible oil rigs in the Gulf of Mexico; see Figures 18 and 20).

Spatial enhancement (SE) was selected over radiometrically enhanced in order to reduce the graininess of the images and make shadows and features, such as waves, more distinguishable. The effective resolution is the primary data quality concern and the modes and designations previously decided upon indicated that we desire spatial enhancement as well.

## 6. PROCESSING METHODOLOGY

Our image processing chain (Figure 5) takes a SAR image, computes *local spectra* (the 2d spectrum of rectangular subimages), and analyzes the resulting spectra to identify wind-driven features. Our approach identifies the local wave direction at a dense grid of points using an angle-valued filter called the Local Spectral Rotation Angle (LSRA), which is an adaptation of the local spectral angle approach developed in [10]. This filter requires a spectral band to be identified – this is derived from manual analysis of local spectra in the image. Using the wave direction computed by the LSRA, the spectral information is reduced to a 1d *range spectrum* that is compared with buoy-derived spectral models to identify the wind speed.

We assume that the spectrum of the height or slope of the ocean surface is reflected in the spectrum of a SAR image of the ocean. Because the SAR image implicitly contains the collection geometry and doppler effects from wave motion, the process of SAR image formation distorts the ocean spectrum. It is well-established that the transformation from ocean spectrum to SAR spectrum is nonlinear, and its inversion is possible via an iterative procedure [12]. Ensuring convergence of this inversion procedure can be difficult, and our implementation of it is incomplete. Because several researchers [12, 3] have found that a quasi-linear approach to inversion is effective, we are currently not performing inversion of the spectrum.

However, this means that the local spectra are subject to nonlinear distortions. For instance, one prominent feature of SAR images of the ocean is that the spectrum suffers a high-frequency cutoff in the azimuthal direction, resulting in spectral energy being confined to a narrow low-frequency band. If one is only interested in the detection of strong gusts, these combined linear and nonlinear distortions do not preclude their visibility.

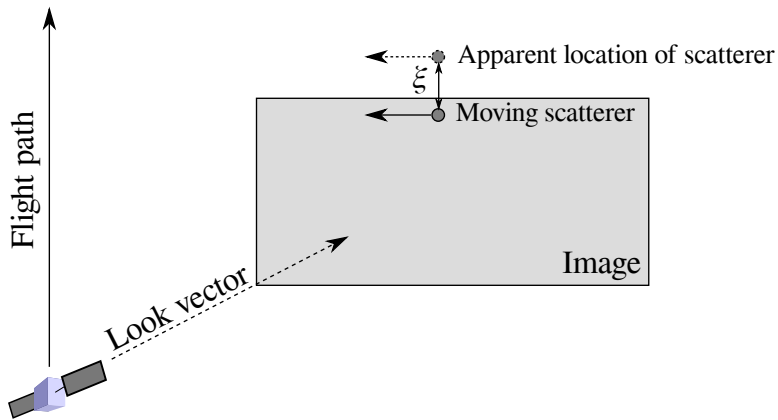


FIGURE 6. Azimuthal displacement of a moving scatterer in the scene

**6.1. Azimuthal cutoff.** Moving objects in a SAR image are displaced from their true position along the azimuthal direction. If a feature in motion is coming towards the satellite parallel to its look direction, the feature appears shifted in the azimuthal direction (same direction as the flight path; see Figure 6). The reverse occurs if the feature is in motion away from the satellite – the feature shifts in the opposite direction of the flight path. When the azimuthal displacement applies to a scene of the ocean, it causes an additional modulation of the waves in the azimuthal direction. The modulation causes evenly-spaced waves to appear “bunched” into groups, which obscures the high frequency content in the azimuthal direction.

Various observations and empirical formulae for the azimuthal rolloff have been proposed, for instance Gaussian cutoff [3] matches the data well. However, [12, Eq. (56)] presented a systematic asymptotic derivation of the azimuthal cutoff factor

$$\exp(-k_x^2 \xi^2), \quad (1)$$

in which  $k_x$  is the azimuthal wavenumber and  $\xi$  is the RMS azimuthal displacement. They tested this formula extensively against SEASAT imagery and found good numerical agreement in about half of the cases they tried.

The azimuthal cutoff formula (1) is a part of a larger programme described in [12] to develop a computational method for converting SAR spectra into wave spectra. We have begun to implement their algorithm for our use on this present project. During the simulation of spectral data during this algorithm development, the images generated during unit testing (for instance, Figure 7) consistently showed features that we hypothesized were related to azimuthal cutoff. We started to see similar features in the simulated ocean height, simulated SAR spectrum, and a  $100 \times 100$  pixel SAR spectral image generated from a subimage.

To validate the azimuthal cutoff formula in TerraSAR-X imagery, one needs an independent measurement of the wave orbital velocity. This datum can be supplied from *in situ* measurements of the height power spectral density of the ocean, if appropriate buoys are available. In our experiment, only NOAA buoy 46089 in the Portland scene has the required capability. Therefore, we will consider validation of the azimuthal cutoff in the case of the Portland images. Table 3 summarizes the

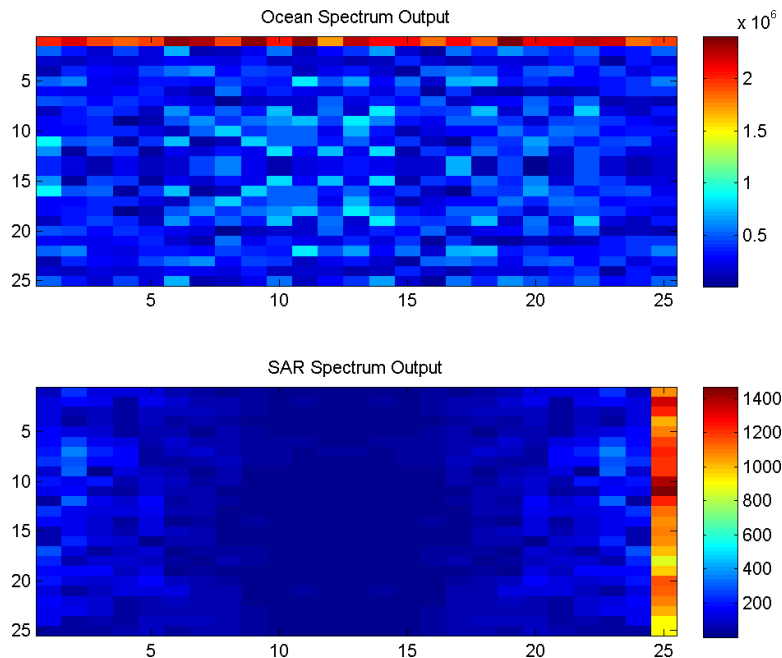


FIGURE 7. Simulated ocean height and SAR spectrum with 2.5 m ocean wavelength

results of our buoy-derived spectral cutoff estimate and its comparison against the cutoffs measured from the two Portland images (Figure 24).

The buoy's record of the power spectral density associated to the ocean surface height distribution at the time of each collection is shown in Figure 8. Assuming the buoy power spectral density  $\Phi(f)$  is a known function of frequency  $f$ , the mean squared height displacement is given by (see [15, 7.3:21])

$$E[h^2] = \frac{1}{2\pi} \int \Phi(f) df. \quad (2)$$

From this, the orbital velocity of a particle on the ocean surface is given by (see [15, 3.3:8.1] or [12, (44)-(45)])

$$E[v^2] = \int f \Phi(f) df. \quad (3)$$

The SAR collection geometry with respect to the wind speed induces a linear modulation of this velocity, namely multiplication by the factor [12, (17)]

$$E[w^2] = E[v^2] (\cos^2 \phi \sin^2 \theta + \cos^2 \theta), \quad (4)$$

where  $\phi$  is the difference between the wind and look direction angles and  $\theta$  is the incidence angle. The first term in the transfer function above corresponds to modulation of the surface velocity, while the second term corresponds to modulation of the vertical component of the velocity. With the modulated mean squared velocity  $E[w^2]$  in hand, the azimuthal displacement  $E[\xi^2]$  can be computed via

$$E[\xi^2] = \frac{R^2}{U^2} E[w^2], \quad (5)$$

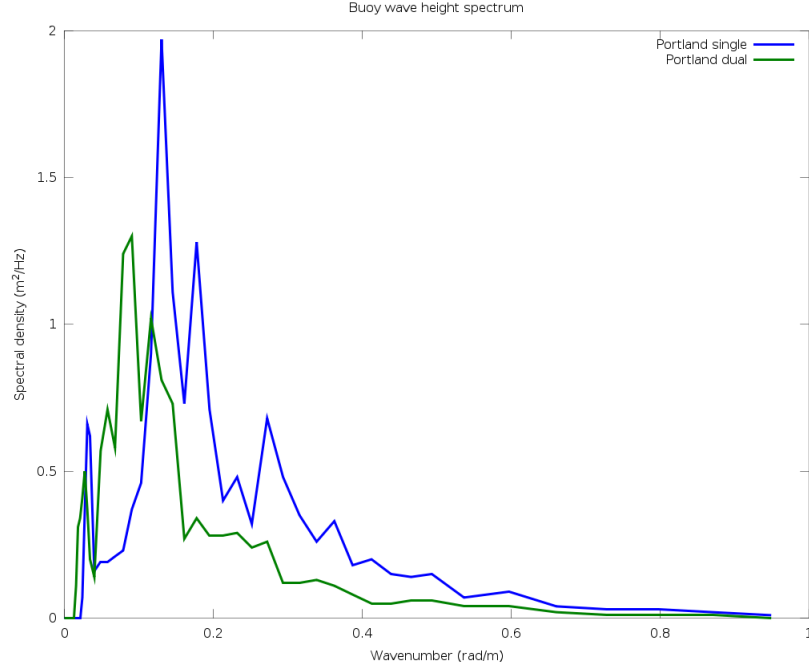


FIGURE 8. Wave height power spectral density as measured by NOAA buoy 46089 coincident with the images

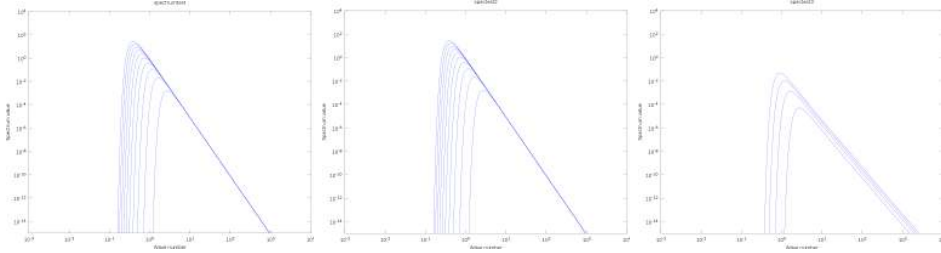


FIGURE 9. Idealized wind wave height spectra from models in [7]

where  $R$  is the slant range and  $U$  is the platform velocity (assuming no crabbing). The 3 dB azimuthal cutoff  $k_x$  can be estimated by solving the equation

$$\frac{1}{2} = e^{-k_x^2 E[\xi^2]}. \quad (6)$$

**6.2. Range spectral models.** To begin our analysis of range spectra, we obtained three theoretical models from [17], each of which was produced from the analysis of accelerometer-derived buoy measurements. These models indicate that the location of the spectral peak changes depending on the input wind speed. Figure 9 demonstrates this phenomenon: as the wind speed increases from 3 m/s to 21 m/s,

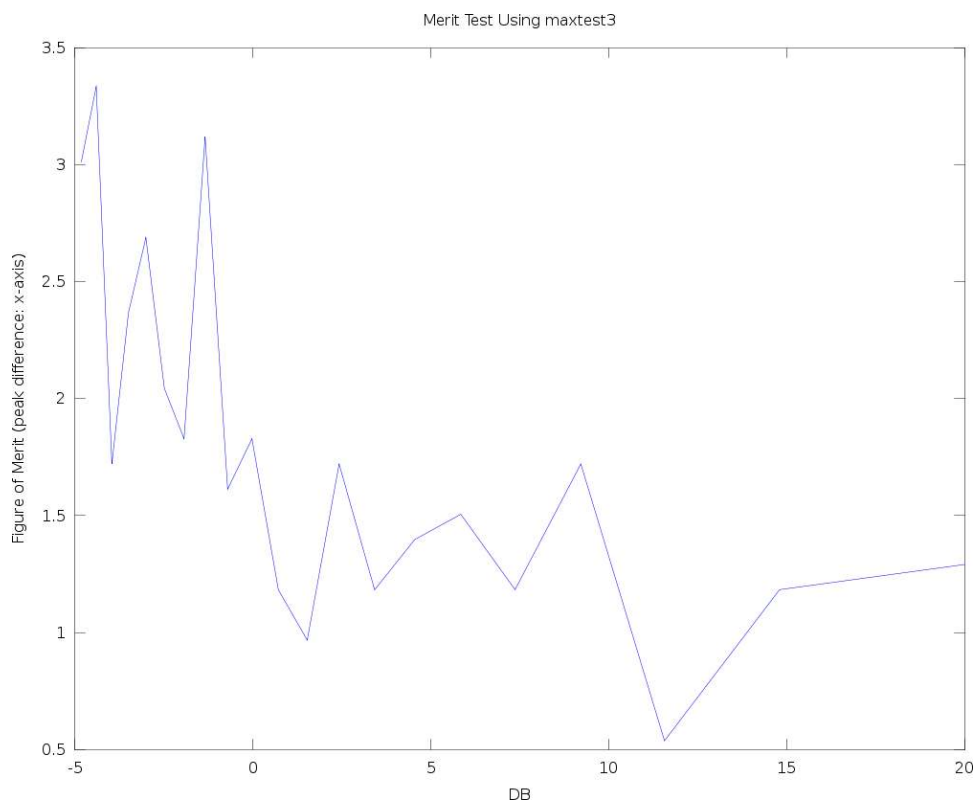


FIGURE 10. Performance of range spectrum parameter fit as a function of addition Gaussian noise level

the location of the spectral peak – and hence, the spectral tail – shifts to the left. We can also see that the peak spectral value itself increases with increasing wind speed, which results in an apparent broadening of the spectrum over the noise floor.

Thus, if we want to invert the process and find wind speed from a given spectrum, we should identify the spectral peak and tail in our analysis of the SAR spectra. We have found that the absolute level of the spectral peak is difficult to assess, so we considered methods concerned with its location in frequency.

We attempted to extract spectra with the proper range of values present in these theoretical models. We did this by identifying spectral gaps in our Fourier transforms of the data. Identifying these gaps was the initial motivation to obtain spectra from various block sizes of the original satellite image (Section 8.2); we altered block sizes in search of a strong spectral peak.

We developed an algorithm to output wind speed given spectral data. The algorithm selected the input values into the theoretical models that gave the best match to the spectral data. This was done through many iterations – testing each possible combination of input values. We used different metrics to determine this best match

- (1) the sum of squared differences of data points,
- (2) the location of the spectral peak in frequency, and

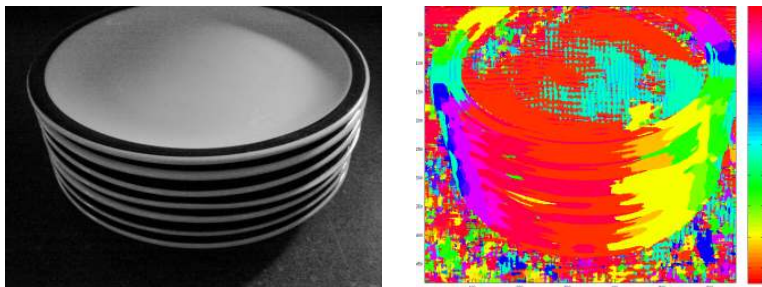


FIGURE 11. An image ( $482 \times 653$  pixels) with curved striations (left) and its LSRA filtered image (right), in which the colors represent angle in degrees. The filter used a block size of 30 pixels and a spectral radius between 3 and 8 pixels.

- (3) the maximum value on each spectral plot.

For each metric, the algorithm gave the wind speed – and other parameter values – that went into the theoretical model.

Before we tested the algorithm on the satellite data, we tested it on ideal noisy data, which we produced by adding Gaussian noise to the theoretical models mentioned above. The algorithm worked successfully on this noisy data. Figure 10 shows how well our algorithm worked against different levels of noise in determining the location of the spectral peak in frequency. (To produce this figure, for each level of noise, we found the mean peak difference over 12 iterations of our algorithm.) In running several tests like this one, we determined that our algorithm worked best with a signal-to-noise (SNR) ratio of about 10 dB or better.

However, our algorithm was not successful in matching – and thus, extracting wind speed from – the experimental data. We believe this is due to the fact that low spectral values were lacking in the satellite spectra; the long “tail” present in the theoretical models were not visible in the actual data. Based on the results in Section 7.1, the actual SNR in the measured data is not much in excess of 10 dB, if at all. Examples of this are presented later in Section 8.3, when we discuss the extraction of a “good” 2-dimensional spectral plot.

**6.3. Visualization of spectral angles.** Waves in the surface of the ocean appear as curved striations in a radar or optical image. This structure is also present in non-ocean images as well. For instance, the left panel of Figure 11 shows a photograph of a stack of dishes. The collection of edges of the dishes forms a striated feature in the image. It is therefore useful to have a filter that measures the orientation of striated features from an image. It is most effective to describe this orientation by an angle.

**6.3.1. Mathematical description.** The local spectral rotation angle (LSRA) filter takes an intensity-valued image to an angle-valued image which enables visual interpretation of striations. Of necessity, this filter is not linear, since the space of angles is not a vector space (it is a group). On the other hand, is local since the orientation of striations changes across the image.

The LSRA filter computes the angle of striations in small patches of an image, and then assembles the resulting computations into an angle-valued image, as shown

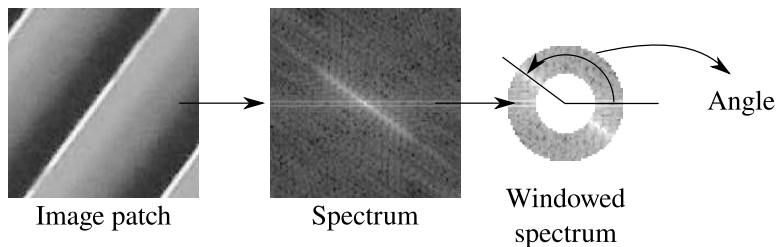


FIGURE 12. Schematic of the local spectral angle calculation

in Figure 12. The LSRA filter uses (1) the 2d-Fast Fourier Transform of a small patch followed by (2) a threshold detection on an annular window to determine the dominant angle.

The LSRA filter takes as input a rectangular grid of  $\mathbb{R}$ -valued pixels (the input image) and four parameters:

- (1)  $M$ , the number of rows in a local patch,
- (2)  $N$ , the number of columns in a local patch,
- (3)  $R_1$ , the minimum spectral radius to test, and
- (4)  $R_2$ , the maximum spectral radius to test.

It produces a new rectangular grid of pixels, for which the value of each pixel is an angle. Collectively,  $M \times N$  is called the *block size* and  $R_1, R_2$  are called the *spectral radii* of the filter.

Specifically, for a  $M \times N$  patch  $s$  of pixels, the local process computes its discrete Fourier transform

$$S(k_x, k_y) = \frac{1}{MN} \sum_{x=0}^{N-1} \sum_{y=0}^{M-1} e^{2\pi i(k_x x/N - k_y y/M)} s_{x,y}$$

for  $k_x = -N/2, \dots, N/2$ ,  $k_y = -M/2, \dots, M/2$ . The local process then computes the frequency coordinates  $(T_x, T_y)$  of the largest spectral component in an annulus via

$$(T_x, T_y) = \operatorname{argmax}_{R_1 \leq \sqrt{k_x^2 + k_y^2} \leq R_2} |S(k_x, k_y)|$$

and returns the angle  $\theta_{x,y} = \tan^{-1} \frac{T_y}{T_x}$  that the dominant spectral component makes with the horizontal. By convention, we assume that  $-90^\circ \leq \theta_{x,y} < 90^\circ$ .

It is important to realize that the direction of the striations themselves is perpendicular to the dominant spectral components. As Figure 12 indicates, the striations (left panel) make an angle of roughly  $45^\circ$  with the horizontal, but the spectral band makes an angle of  $-45^\circ$  with the horizontal.

**6.4. Noise performance of spectral angle measurement.** In this section, we explain a method for testing the LSRA filter and quantifying its precision and accuracy. Based on the imagery we collected, it appears that a pixel radar cross sections are lognormally distributed (Figure 21).

We generated an  $M \times N$  pixel simulated image using the following formula

$$s_{i,j} = \cos \left( \frac{i}{M} \cdot k \cos \theta + \frac{j}{N} \cdot k \sin \theta \right) + n_{i,j}$$

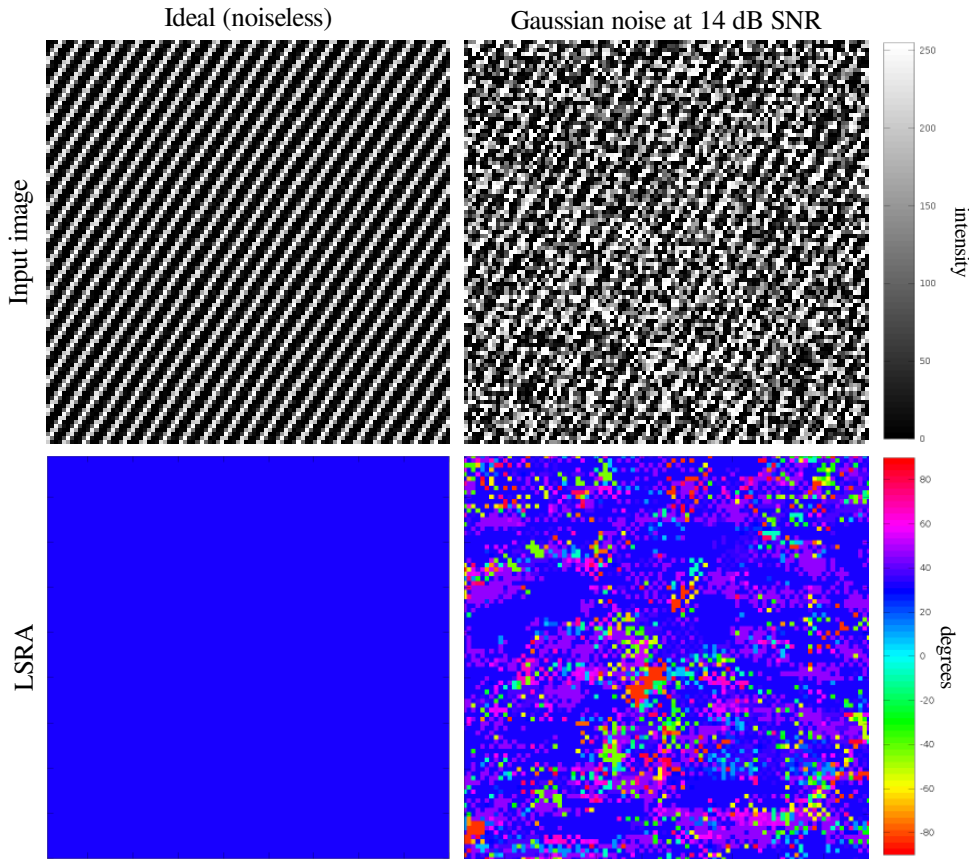


FIGURE 13. Sample Ideal Function (Top Right), Sample Simulated Additive Gaussian Noise Image (Top Left), Output of LSRA for Ideal Image (Bottom Right) and Output of LSRA for Image containing Noise.

to give the intensity of the  $i$ -th row and  $j$ -th pixel under the assumption of zero-mean, uncorrelated additive gaussian noise  $n$ . We iterated over various values for the noise variance, the wave number  $k$ , and the angle of the waves  $\theta$ . Two such exemplars with different noise levels are shown in Figure 13.

For this analysis we used  $100 \times 100$  pixel images to reduce run time and allow for hundreds of simulations to be run in a reasonable time. When running the algorithm on these smaller images we used a block size of 10 pixels, minimum spectral radius of 2 pixels and maximum spectral radius of 8 pixels. Comparing the results of our algorithm from the ideal image with the results of the noisy image generates the Receiver Operating Curves shown in Figure 14. This plot indicates a sharp improvement in angle estimation performance when there is sufficient signal to noise ratio. We note that the curves shown may be pessimistic, since the block sizes chosen are rather small.

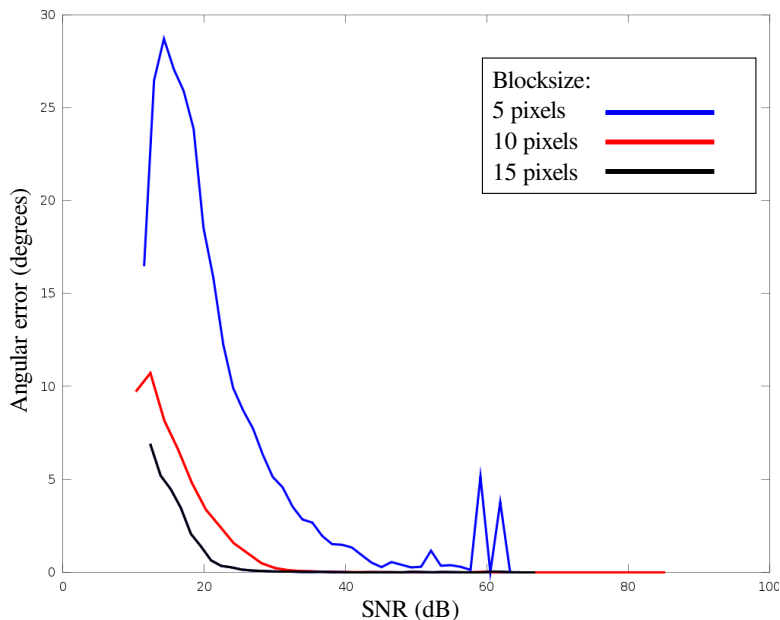


FIGURE 14. Angular estimation error using LSRA on an image with additive Gaussian noise

TABLE 2. Overview of data collections

Date	Time (UTC)	Region	Polarization	Pass direction	Incidence
2013-04-23	12:00	Gulf	Dual	Descending	42°
2013-04-24	00:05	Gulf	Single	Ascending	44°
2013-04-24	14:30	Portland	Single	Descending	44°
2013-04-28	02:11	Portland	Dual	Ascending	38°

## 7. DATA OVERVIEW

We acquired four images (see Table 2) centered on two locations. At each location, we acquired a single and a dual polarization image to assess both the value of polarization data and temporal variability of the imagery.

For the Portland scenes, we note several key observations. First, no obvious vessels are present in either scene. In the dual-polarization image (Figures 15 and 16), we detected two areas of note: (1) a calm area (top right frame of Figure 15) and (2) a turbulent downdraft (bottom right frame of Figure 15). Apparent in the single-polarization image (Figure 17) were streaking features, parallel to the wind direction. While the buoys selected for ground truth did not appear in the scene – we suspect the coordinates supplied by the National Data Buoy Center may be inaccurate – there is live data from the appropriate buoy.

Due to the myriad of organizations exploiting the oil reserves of the Gulf of Mexico, much human activity is present in the Gulf scenes (Figures 18 through 20). Though inevitable, it is prudent to avoid boats and platforms as much as possible, recognizing that most of the “buoys” providing richer data are actually anchored

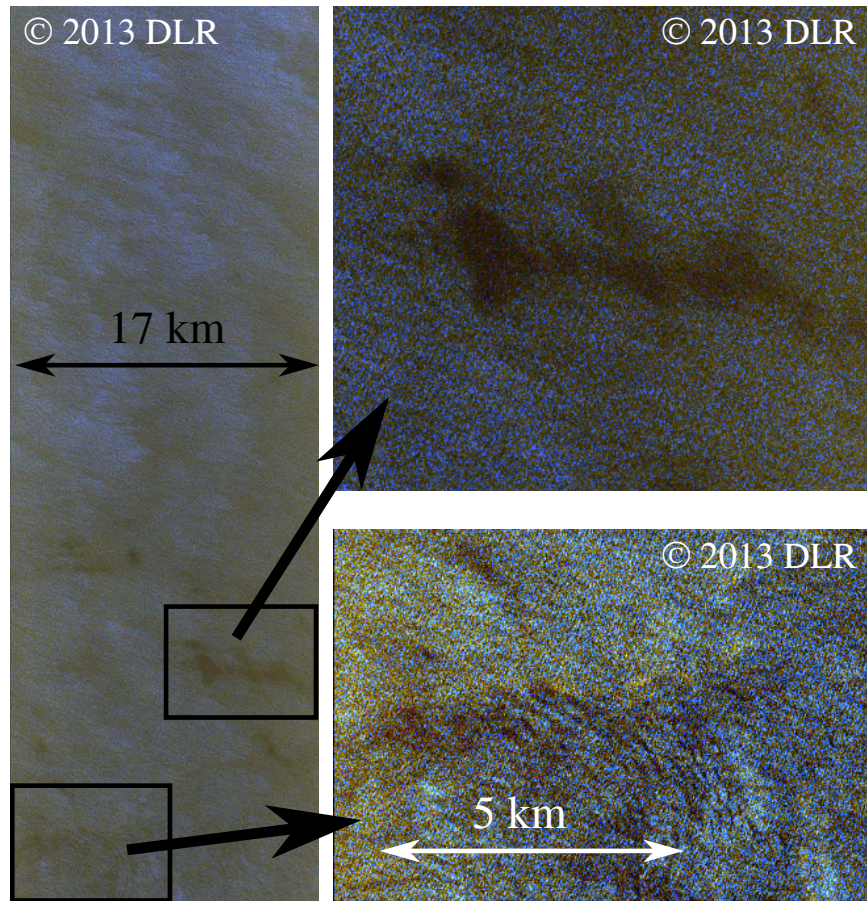


FIGURE 15. The entire Portland dual scene (all polarization composite) with two wind-driven features. Top right frame: a region with lower wind speed; bottom right frame: an apparent downdraft

platforms. In this particular image, the ocean current seems to have the most effect on the surface texture. The effect of the wind on the surface texture is visible at a higher zoom level (see Figure 19).

**7.1. Pixel radar cross section distribution.** The histograms of the radar cross sections (RCS) for each pixel in each image are shown in Figure 21. These demonstrate that the distribution of pixel RCS values from each image is approximately log normal, though a bit more central. This is consistent with the findings of other researchers, for instance [21] describes sea surface clutter as being gamma distributed.

**7.2. Qualitative of overview of local spectra.** After looking at several typical spectra (for instance Figure 22), it appears that the inclusion of boats and other structures yield high noise and a great deal of irregular spectral shapes. This results from boats and other metal objects having higher reflectivity and localized structure within the image. The obstruction caused by these objects makes LSRA

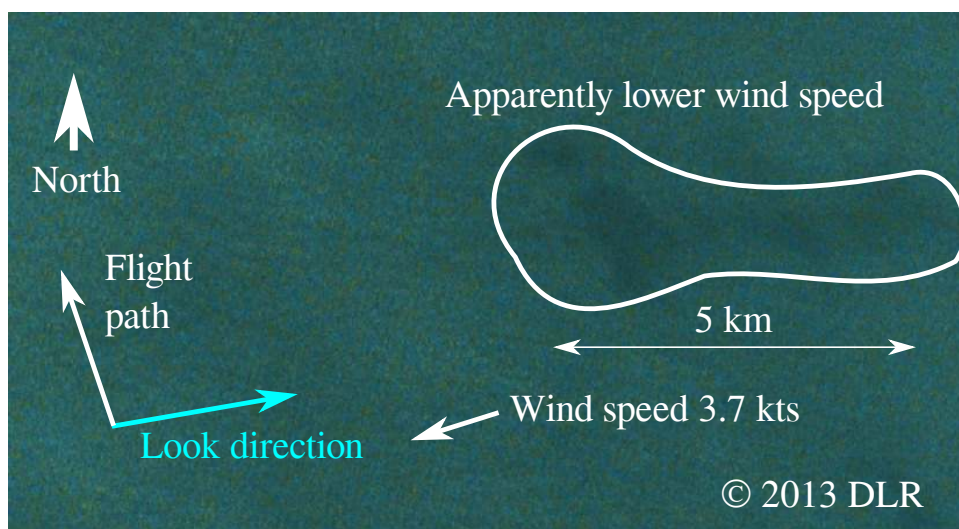


FIGURE 16. Detail in the dual-polarized Portland image (28 April 2013)

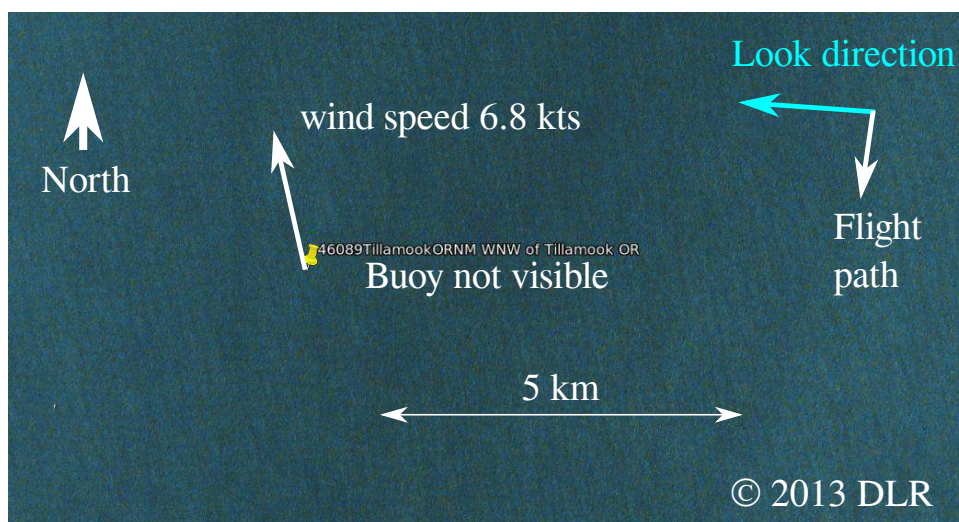


FIGURE 17. Detail in the HH-polarized Portland image (25 April 2013)

images harder to interpret, so more processing is required to excise them from the imagery. Thus we will avoid boats, platforms, and other artificial interference they may bring.

## 8. DETAILED ANALYSIS OF SPECTRA

**8.1. Validation of azimuthal cutoff.** In order to verify the azimuthal cutoff formula from [12], we implemented several spectral and metadata manipulation stages. Namely, the paper proposes a forward process that takes an ocean spectrum

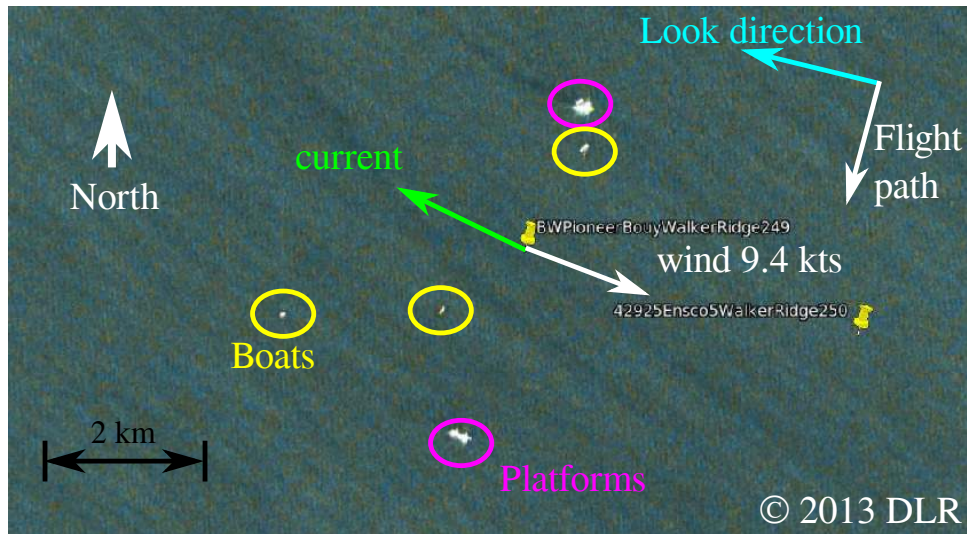


FIGURE 18. Detail in the dual-polarized Gulf image (23 April 2013)

and yields a SAR spectrum, and an inversion process to find an ocean spectrum based upon an input SAR spectrum. We verify the azimuthal cutoff using the output of these processes.

The forward process from the paper involves two main components. First there is a frozen surface contribution that uses tilt and hydrodynamic modulation transfer functions (MTF) to synthesize a real aperture radar MTF. From there the contribution of any frozen surface can be explained by the surface elevation and this new MTF. The second component, motion effects, allows the SAR to be corrected as to the movement of the waves. In particular, the motion effects take into account a new velocity bunching MTF. With these two components, an integral formulation builds the SAR intensities from image data, resulting in a SAR spectrum.

The process of building an inversion program, while following the paper's formulae, has been somewhat more challenging. In particular, there is an iterative integration that takes much longer to run and requires considerably more parameters as input. It was decided that venturing into azimuthal cutoff verification might yield insights into this inversion, in parallel with our implementation of the algorithm.

In order to compute the azimuthal cutoff, a metadata parser was developed that parses the XML-formatted files supplied with the imagery. The parser computes the minimum slant range from twelve ephemeris points on the satellite's flight path, measured from the image center. That slant range is then fed through the velocity MTF and used in a computation of the mean square azimuthal displacement, which is in turn fed through the azimuthal cutoff term expression. Additionally, the parser's implementation generates diagrams (for instance Figure 23) that show the collection geometry, including buoy-derived vectors for wind, waves, and current when available.

Since buoy-derived spectra were only available from the buoys near the Portland scene, we estimated the azimuth spectral cutoff wavenumbers using the procedure

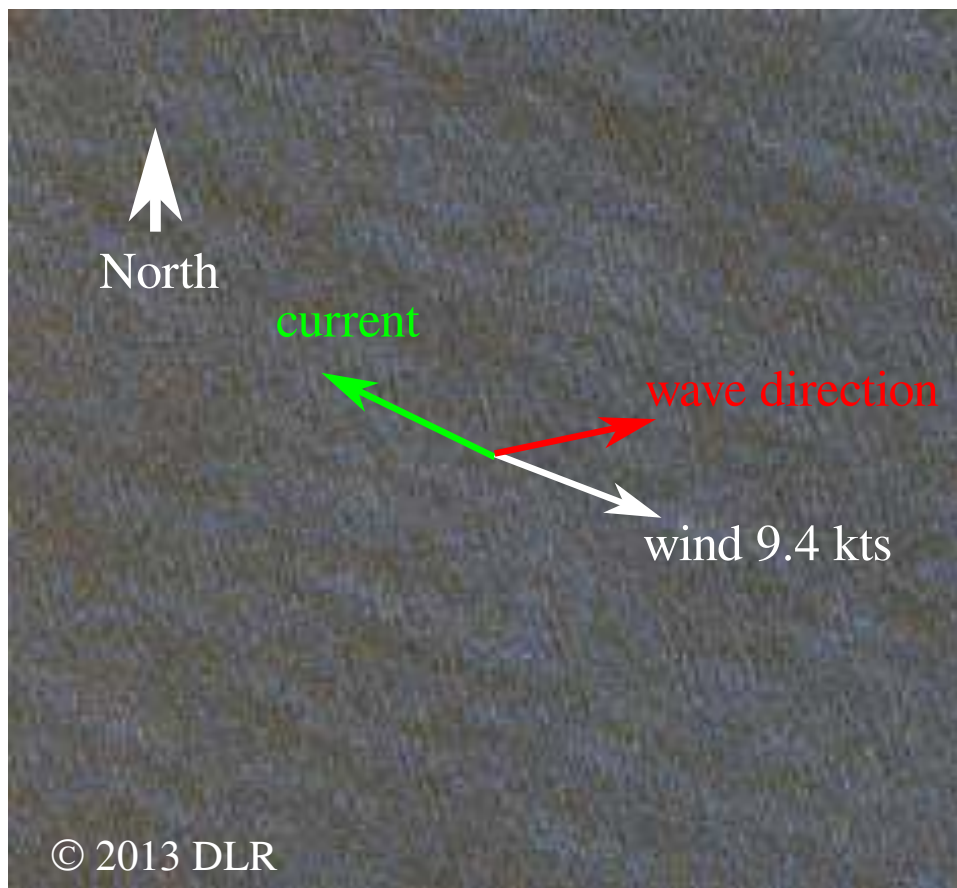


FIGURE 19. Detail in the dual-polarized Gulf image (23 April 2013), showing current direction (from buoy), wind direction (from buoy), and surface waves (visible in image). Image is roughly  $3 \text{ km} \times 3 \text{ km}$ .

described in Section 6.1 for each of the two Portland images. The results of our calculations are summarized in Table 3. For each image, we selected an area free of visually-apparent turbulence in order to estimate the 3dB spectral width in the azimuthal direction. Since we performed these measurements manually by inspecting an image, we suspect that there is a margin of error of approximately 5–10%. The spectral width measured from the Portland single polarization image agrees with the buoy estimate to within 3%, so appears to validate the cutoff formula. However, the Portland dual polarization image shows a larger disagreement than our measurement error, which could possibly be traced to the fact that the image shows more turbulence (and subsequently more spectral variability) than the single polarization image. Had the buoy been actually visible in the image, we suspect that a more close agreement could be possible.

**8.2. Spectral block size study.** In order to determine the appropriate block size for spectral estimation, we processed the data from each image, using block sizes

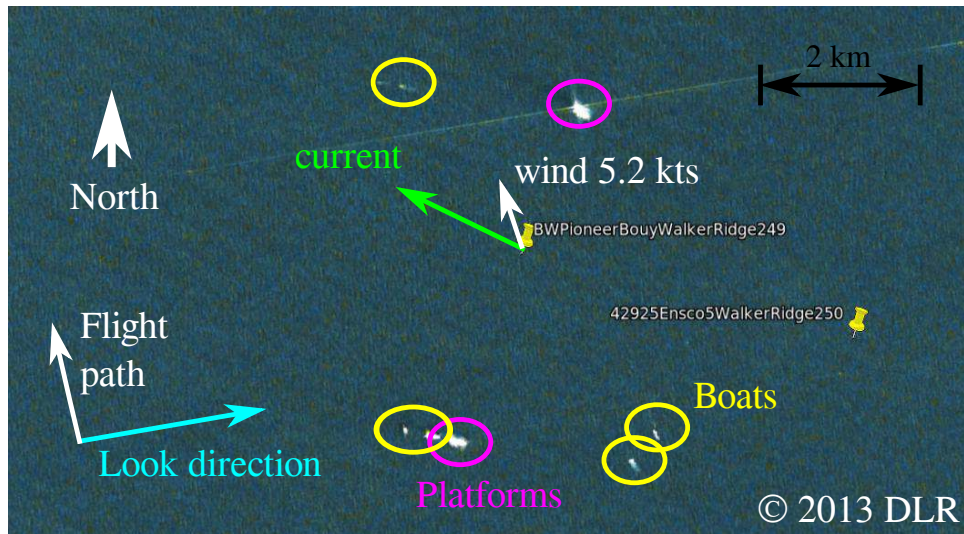


FIGURE 20. Detail in the HH-polarized Gulf image (24 April 2013)

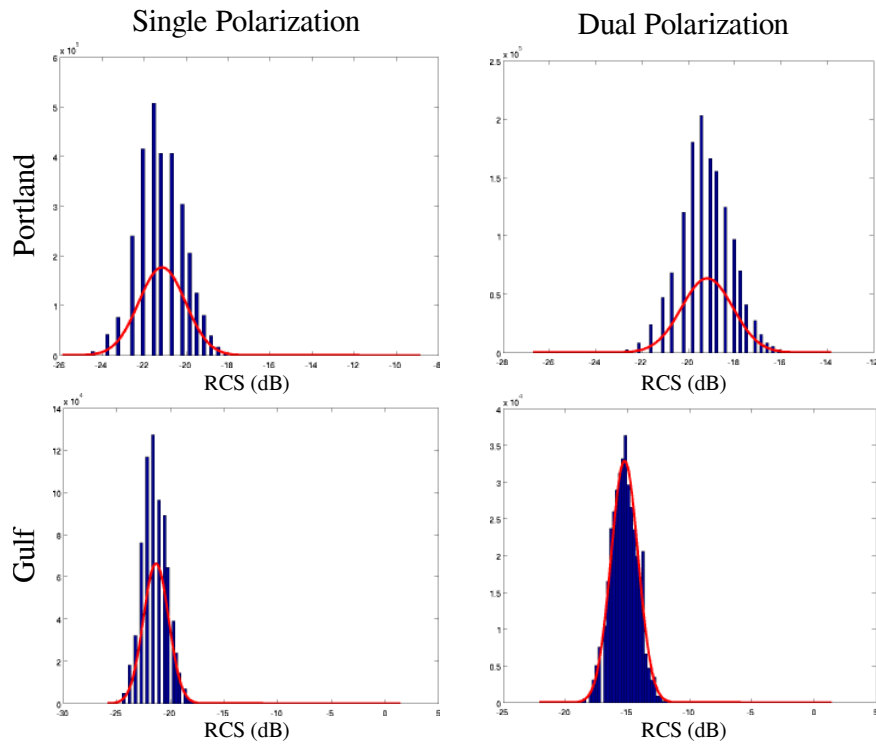


FIGURE 21. Histograms of calibrated pixel RCS values in a uniform region from each image. Best-fit lognormal distributions are shown in red on each.

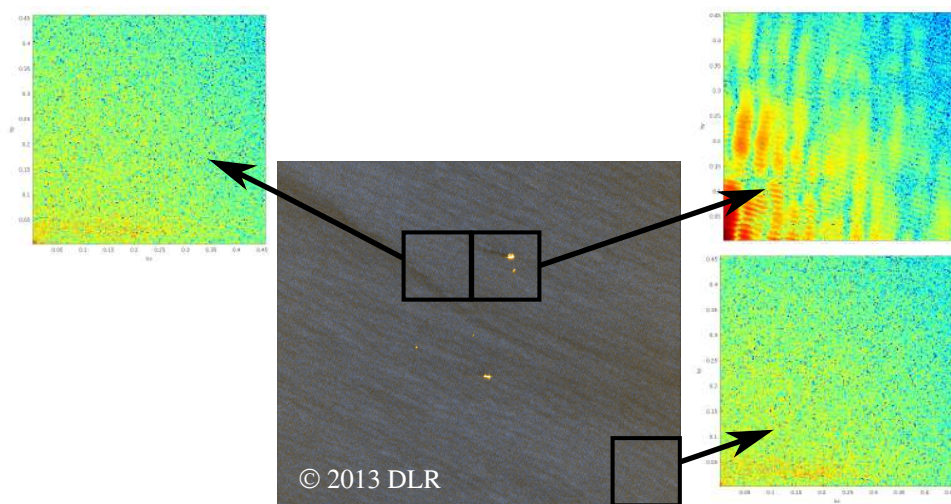


FIGURE 22. Several local spectra of the VV-polarization of the Gulf dual image

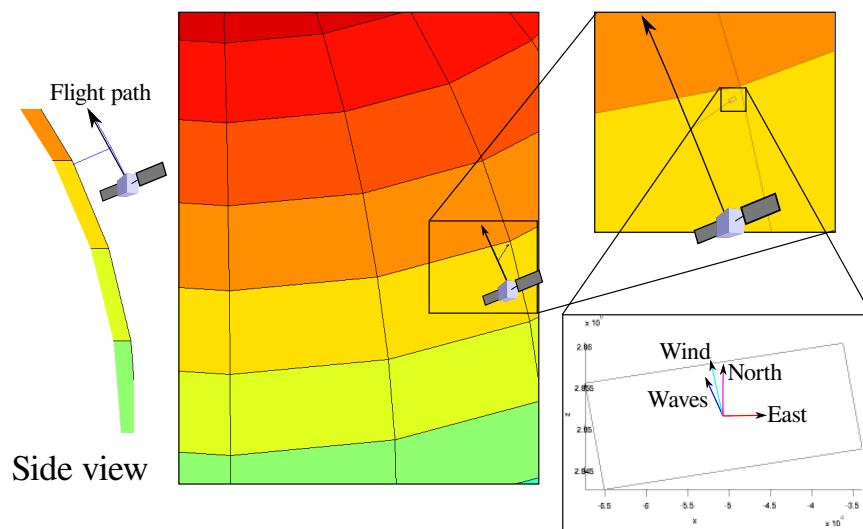


FIGURE 23. Overview of the collection geometry, wind, and current conditions for the Portland single image

from 100 to 5000 pixels. In doing this, we were looking for both the presence of high spectral values and the clarity of the spectral gap. Each processing block was formed from the upper corner of the collected images as shown in Figure 25, because these happened to be relatively free of turbulence and human activity.

We found that at a block size of around 200 pixels (500 m), we can start to see higher spectral values localized into a spectral peak. Around 700 pixels (2 km), the spectral peak is consistently well-defined, if present, and one can also begin to see

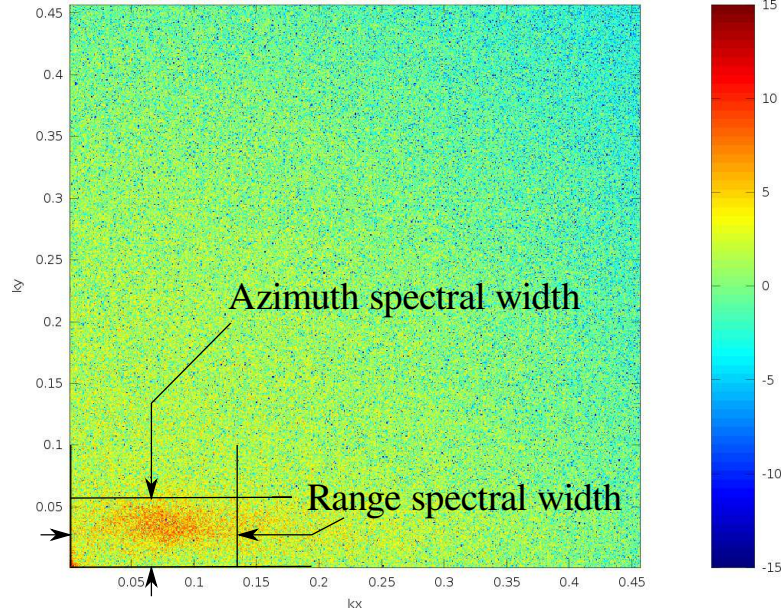


FIGURE 24. Zoomed in spectrum (Portland dual VV polarization) showing the measurement of spectral widths

TABLE 3. Summary of azimuthal cutoff calculations

Parameter	Source	Portland single	Portland dual	Units
Spectral peak	Buoy	0.13	0.09	rad/m
Wind direction	Buoy	350°	262°	deg true N
RMS displacement	Eq. (2)	0.15	0.14	m
RMS orbital velocity	Eq. (3)	0.21	0.16	m/s
Slant range	DLR	796	700	km
Satellite speed	DLR	7.7	7.7	km/s
Incidence angle	DLR	44°	42°	deg from vert
Look direction	DLR	260°	91°	deg true N
Az. displacement	Eq. (5)	15.5	14.3	m
Az. cutoff	Eq. (6)	0.053	0.058	rad/m
Az. cutoff	Image	0.055	0.050	rad/m
Percent error		-2.3%	16%	

a well-defined spectral gap. It is not until we utilize a block size of around 2000 pixels (5 km), however, that we *consistently* see a clear spectral gap. These results are summarized in Table 4.

**8.3. Analysis of 1d spectral cuts.** In order to compare the spectral values that arose in our data with the theoretical models (for instance [7, 17]), we needed to extract them along a line from the local spectra. We did this by extracting spectral values along lines of various slopes going through the origin, giving each line its unique spectral graph. Figure 26 shows an example of a spectral graph formed by

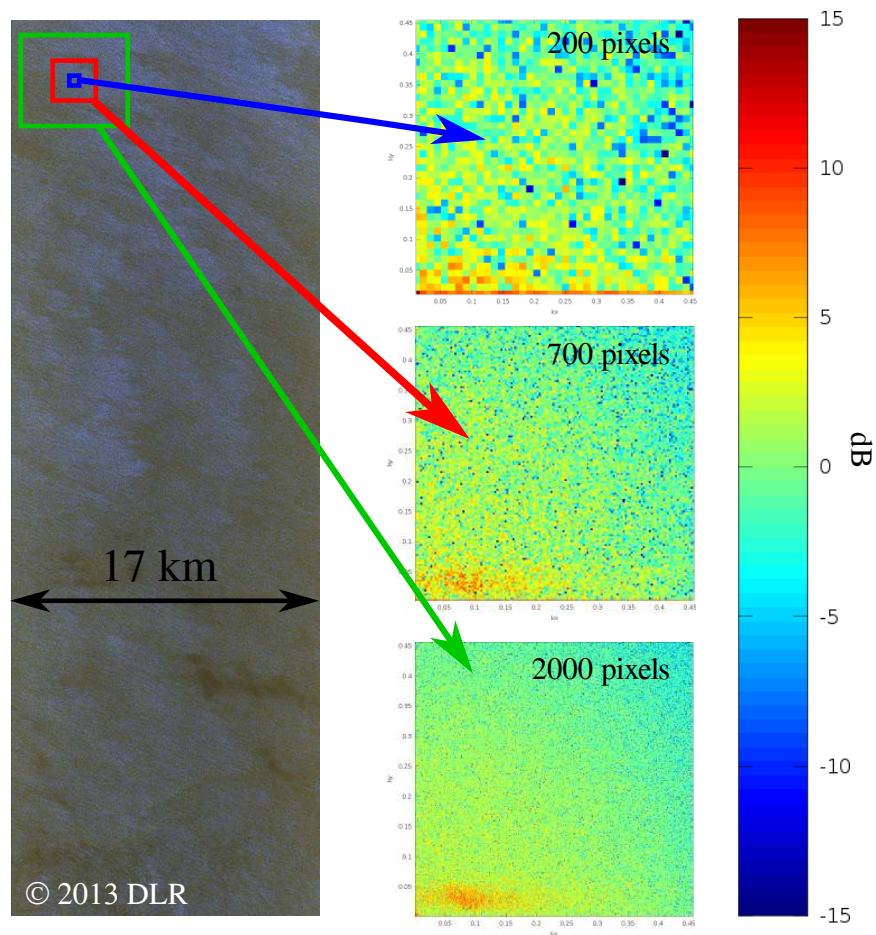


FIGURE 25. The DLR-supplied preview image of Portland dual (left) and spectra measured at a single location with varying block sizes (right)

TABLE 4. Qualitative wind feature performance

Resolution	Spectral features visible	Measurement implication
500 m	Sporadic spectral peaks	Direction of strong waves
2 km	Consistent spectral peak	Direction of all waves
5 km	Spectral gap visible	Wind speed (speculative)

using the data along the one-dimensional line shown in the spectral image. The spectral frequency was plotted against the corresponding angular frequency for that data point under the assumption of a deep water dispersion relation.

Of the spectral graphs we extracted, we are looking for those that best match the theoretical models from buoy data. These “good” graphs would have a well-defined

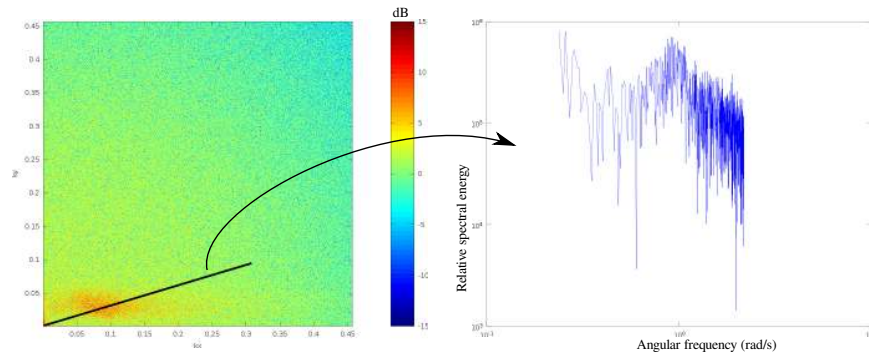


FIGURE 26. A 2d spectrum (left) taken from an image, and the 1d spectrum along a cut in the range direction (right)

peak and tail. However, as previously mentioned, the tails were not long enough to match up well with the theoretical models.

The best graphs came from lines of various slopes, but they were almost always between 0 and 0.5 – probably due to the collection geometry and wind conditions during our collections. Typically, the best results were obtained with a block size of around 3000 pixels. It was difficult to generalize when a “good” graph would arise, but it is clear from Figure 26, for instance, that the line associated with the graph goes through a decent portion of low spectral values as well as through the concentrated mass of higher spectral values. Our goal for the future is to statistically determine what a truly “good” graph should be, based on an analysis of spectral values in the dense high-frequency spectral patch.

**8.4. Spectral spatial variability study.** After keeping our spectral analysis fixed on a certain corner of an image, we decided to perform a sweep over the entire image using block sizes from 1000 to 5000 pixels, and then later from 200 to 1000 pixels. This allowed us to see certain features that were consistent across the entire image, as well as to see whether these features appeared in our use of different block sizes.

This analysis was especially useful in the Portland image (with vertical polarization), since it allowed us to focus on its interesting features. As Figure 15 shows, there are a few interesting features in this image, one of which is the apparent downdraft in the bottom-left corner of the image, the other of which is a prominent “dark spot” in the lower-middle portion of the image. Figure 27 shows the spectra within these features, as well as the spectrum of a “normal” patch of ocean. As one might have guessed, the spectral features seem to die out over the dark region. Compared to the “normal” image, we see that the high spectral values nearly completely dissipate. Over the downdraft, we see that the spectrum scatters a little bit, possibly indicating a swirling wind – the wind direction is not well-defined in this area.

In our sweep of the Gulf image (with vertical polarization), we found that throughout the image, the highest spectral values were oriented horizontally, indicating that the waves have a constant horizontal direction throughout the image (see Figure 22). We can also see that the spectral values are spread out along higher wave numbers than those from the Portland images. This may be due to the fact

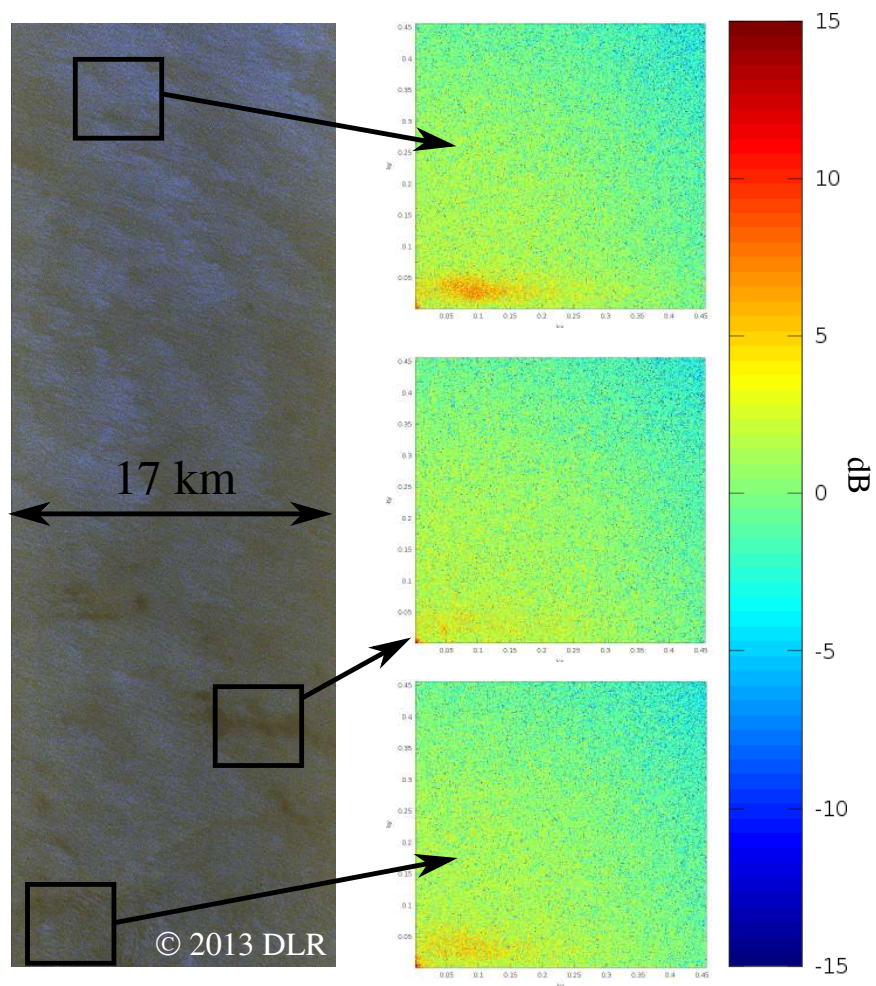


FIGURE 27. The DLR-supplied preview image of Portland dual (left) and spectra measured at several locations of interest (right)

that wind speeds were higher in the Gulf region at this time, according to our buoy data. That is, from our initial discussion of the theoretical models of wave spectra, we saw that the higher the wind speed, the more spread out the spectrum was along the frequency axis. Thus, our results are in line with the theoretical buoy models in this respect.

In Figure 22, we also present what happens to our spectral analysis when a boat (or something else) appears within a processing block. As expected, the presence of the boat prohibits us from saying anything about the behavior of the waves in that block.

## 9. ANALYSIS OF LSRA FILTERED IMAGES

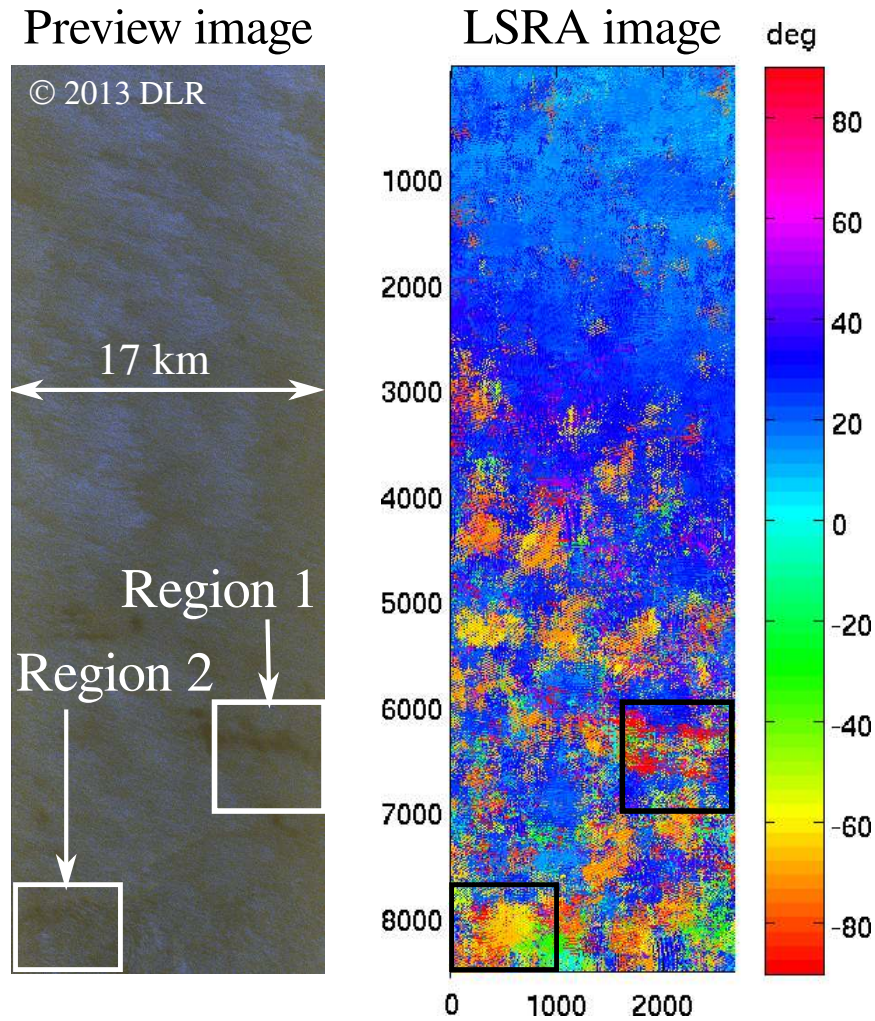


FIGURE 28. The DLR-supplied preview image of Portland dual (left) and the resulting LSRA image with two regions of interest marked. (Axis labels are in pixels, with one pixel being 2.75 m on a side.)

**9.1. LSRA filtered image highlights.** The left frame of Figure 28 is the DLR-supplied preview image of the Portland dual polarization scene. It shows the general idea of how the ocean wind looks like, but we cannot interpret the wind direction and the speed directly from the image. We processed the image into local spectral angles using the LSRA filter described in Section 6.3.1, and present the angle-valued image as a new colored picture, shown on the right of Figure 28. The advantage of the LSRA image is that it shows the wave direction in high spatial detail compared to the traditional ocean wind direction report, which cannot resolve transient wind features.

In the Portland dual polarization LSRA image, the upper portion of the image is very stable and it is mostly around  $30^\circ$ . The lower part of the image is very unstable and the wave direction varies from  $-90^\circ$  to  $90^\circ$ . We focused on two regions in the scene: Region 1 is an apparent calm area, and Region 2 appears to be a large downdraft. We analyzed these two regions by comparing their preview image, local spectra of subimages and LSRA-processed images. In Region 1, there is a large area of the LSRA image which is shown in red, which stands for  $90^\circ$ . It appears that the wind direction is mainly pointing to the north. The downdraft feature in Region 2 is not very visible in the image domain when viewed at a low resolution. However, after processing with LSRA, we see a large coherent feature in Region 2 whose colors vary slowly over its extent, which indicates a radiating pattern of waves in that region. To verify the presence of this feature, we went back to the preview image and zoomed in on Region 2, and found a rather striking pattern of waves radiating from a central point. *The LSRA process helped us to detect a transient wave feature that cannot be seen easily in the original satellite image.*

**9.2. Polarization comparisons.** The experimental campaign described in this report was intended to be a preliminary collection in preparation of a larger one. One of the questions we wished to address is whether higher resolution or polarization diversity was more desirable, since obtaining additional polarization images degrades the resolution that TerraSAR-X provides. We found that *resolution is not a driving factor, while polarization diversity is crucial*. In particular, the wind driven spectral features we need to resolve in order to determine wind speed occur at low wavenumbers (Section 8.2). Higher wavenumbers are required for wind direction estimation, but the dual polarization products appear to have sufficient resolution to extract suitable estimates.

In a side-by-side comparison of polarization images, *VV-polarized image products are substantially better for detecting subtle wind-driven features in the ocean surface*. Consider the dual-polarized Portland image in Figure 29. Both HH and VV polarization show spectral angle variations consistent with increasing turbulence in the south (bottom) portion of the image. However, the VV polarization image resolves the transient wind features (boxes), but HH polarization does not.

In the dual-polarized Gulf images (Figure 30), there are no apparent transient wind features, but the HH polarization image shows markedly higher background speckle level than is present in the VV polarization image.

**9.3. LSRA window tuning study.** In addition to processing block size, Section 6.3.1 explains that there are two additional parameters that control the operation of LSRA: the minimum and maximum spectral radii. These parameters control the visibility of angle-related features of the ocean surface; ideally they should be chosen to bound the ocean spectral peak. The direction-relevant portion of the spectrum is localized in wavenumber magnitude and angle – not selecting the proper band of wavenumber magnitudes leads to incorrect directional estimates. Poor estimates of wave direction result in image products in which the wind dynamics are not visible, and are typically rather heavily speckled (left frame of Figure 31). Of course, if the spectral peak’s location is unknown, we cannot select these parameters *a priori*, but need to estimate them in a data-driven way.

We settled on an experimental procedure based on adjusting the parameters manually to minimize the background speckle over the entire image. For instance,

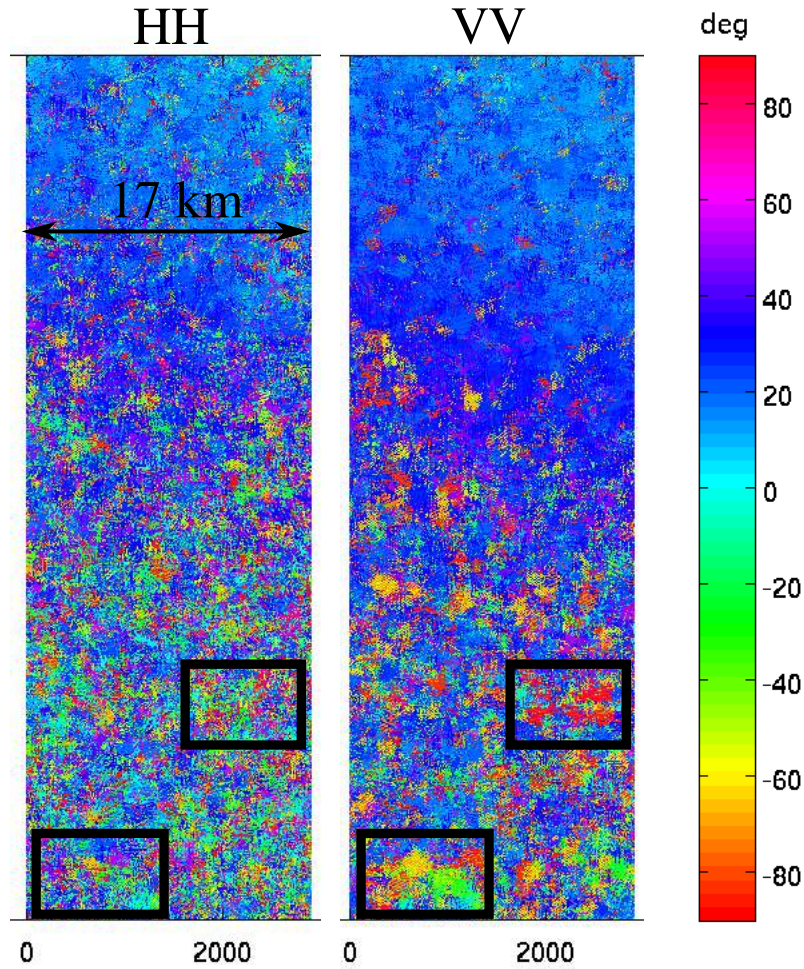


FIGURE 29. Comparison of the LSRA images produced using HH (left) and VV (right) polarizations of the Portland dual image. (Axis labels are in pixels, with one pixel being 2.75 m on a side.)

Figure 31 shows an inappropriate (left) and appropriate (right) choice of LSRA parameters. We have generally found that the best ratio between the minimum spectral radius and blocksize is around  $1/50$  and the best ratio between the maximum spectral radius and block size is around  $1/10$ .

#### 10. NEXT STEPS

We intend to proceed in several directions, addressing each of the following three areas:

- (1) Validation – comparing the data already collected against models and other measurements,
- (2) Collection – acquiring a new, refined dataset from TerraSAR-X, and
- (3) Algorithm development and implementation.

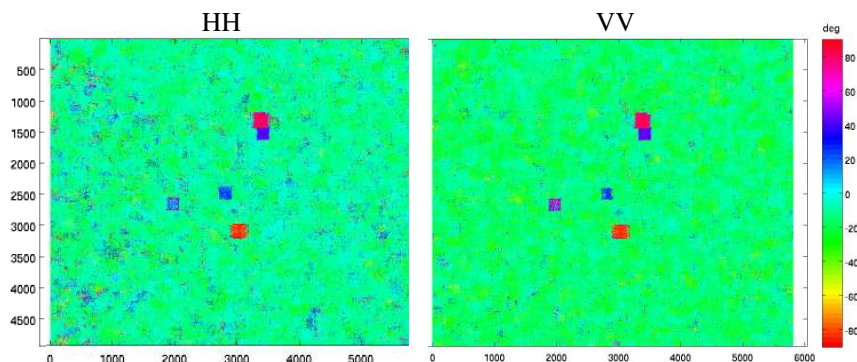


FIGURE 30. Comparison of the LSRA images produced using HH (left) and VV (right) polarizations of the Gulf dual image. The square features in the images are boats and platforms. (Axis labels are in pixels, with one pixel being 2.75 m on a side.)

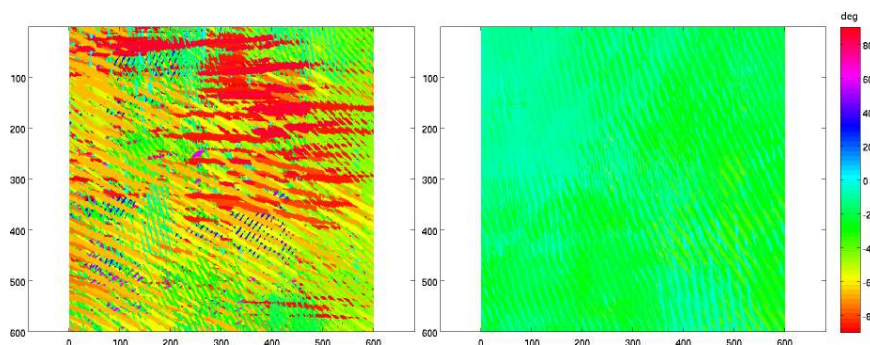


FIGURE 31. LSRA filtered subimages from the Portland dual VV image with a blocksize of  $400 \times 400$  pixels, and a spectral window of 8 – 20 pixels (left), 10 – 40 pixels (right). (Axis labels are in pixels, with one pixel being 2.75 m on a side.)

10.1. **Validation.** Bearing in mind that there is wind turbulence present in some of the images, we intend to compare the LSRA angular estimates against two primary sources of data: the buoy records of wind and current directions, and near-coincident collections from other satellites (primarily scatterometers). Each of these present some challenges because of the rather substantial difference in resolution between our products and others. In particular, differences in collection time may preclude comparison with other sensors. Additionally, we will need to incorporate the effect of surface currents in the ocean in order to determine an accurate wave direction. Unfortunately, none of the buoys we selected provide current direction and wave spectrum simultaneously. For those buoys that provide wave spectra, it remains to perform a more careful comparison of these with our spectral estimates after performing the appropriate transformations from the SAR spectral domain to the ocean spectral domain.

TABLE 5. Potential buoys to be used as future scene centers

Region	Number	Name
Gulf	NOAA 42020	Corpus Christi, TX
Portland	NOAA 46087	Neah Bay
Portland	NOAA 46088	New Dungeness

We also intend to increase our understanding of the theoretical performance of LSRA under realistic clutter and wave models. In particular, we hope to extend our analysis by manipulating the block size and spectral radii, attempting to identify heuristics that handle additive noise better. Based on the results we hope to find a relationship between the size of the image and the blocksize that reduces runtime while still providing a high level of accuracy and precision. Additionally, we will incorporate a realistic model (for instance, one of those suggested in [21]) of speckle in each simulated image. Speckle represents the interference of the returning wave packets and have been shown to be modeled accurately with a Rayleigh distribution. Performing these two additional simulations should validate the robustness of the developed algorithm LSRA.

**10.2. New data collection.** We intend to submit a new data request to TerraSAR-X in the beginning of 2014 that will focus on a dual-polarization, repeat-pass collection campaign. As our study of the data collected thus far indicates, VV polarization appears to be especially valuable, though we would like to quantify that difference, and determine if there are cases in which HH polarization is more useful. Because temporal variability is an important aspect of weather monitoring and prediction, a repeat-pass sequence of images (probably five to seven images in total) will provide an initial assessment of this variability.

We will probably center the images on one of the buoys listed in Table 5, since these are some of the very few that appear to supply all of the data we believe we need. Although high resolution is not necessary for identifying the spectral gap (and hence wind speed), it may be useful for refined estimates of wind direction. Because of this, we may direct our data request to the new high resolution opportunity (New Modes of TerraSAR-X 2013).

**10.3. Algorithm development.** We have thus far focused on processing the TerraSAR-X data using essentially well-understood methods. This has reduced our project’s overall risk, and has allowed us to become familiar with the data and some of its particulars. However, we believe there is substantial unexploited potential beyond spectral processing, based on our group’s theoretical work on topological filters [23]. Analysis of local spectra is an effective methodology when there is both enough wave visibility and waves are locally linear over the averaging windows. However, transient wind features vary substantially in their reflectivity and their wave crests are not necessarily linear over the windows to acquire enough signal for detection. Topological filtering may lead to a systematic way to describe the spatial variability of these transient ocean surface features.

#### REFERENCES

- [1] Joan Ulrich Von Ahn. The impact of QuikSCAT winds on the issuance of marine wind warnings. *Mariners Weather log*, 47(2), December 2003.

- [2] Miguel Bruck and Susanne Lehner. Coastal wave field extraction using terrasars-x data. *Journal of Applied Remote Sensing*, 7(1):073694–073694, 2013.
- [3] Fabrice Collard, Fabrice Ardhuin, and Bertrand Chapron. Extraction of coastal ocean wave fields from SAR images. *Oceanic Engineering, IEEE Journal of*, 30(3):526–533, 2005.
- [4] Guillermo M Diaz Mendez, Susanne Lehner, Francisco J Ocampo-Torres, Xiao Ming Li, and Stephan Brusch. Wind and wave observations off the south pacific coast of mexico using terrasars-x imagery. *International Journal of Remote Sensing*, 31(17-18):4933–4955, 2010.
- [5] P. DiGiacomo, L. Washburn, B. Holt, and B. Jones. Coastal pollution hazard in southern California observed by SAR imagery: stormwater plumes, wastewater plumes, and natural hydrocarbon seeps. *Marine Pollution Bulletin*, 2004.
- [6] DLR. TerraSAR-X image of the month – the coastal cliffs of Christmas Island. [http://www.dlr.de/dlr/en/desktopdefault.aspx/tabid-10081/151\\_read-5978/year-all/#gallery/8506](http://www.dlr.de/dlr/en/desktopdefault.aspx/tabid-10081/151_read-5978/year-all/#gallery/8506), January 2013.
- [7] T. Elfouhaily, B. Chapron, and K. Katsaros. A unified directional spectrum for long and short wind-driven waves. *J. Geophys. Research*, 102(C7):15781–15796, July 1997.
- [8] Geir Engen, Paris W Vachon, Harald Johnsen, and Fred W Dobson. Retrieval of ocean wave spectra and rartf’s from dual-polarization sar data. *Geoscience and Remote Sensing, IEEE Transactions on*, 38(1):391–403, 2000.
- [9] Center for Satellite Application and Research. <http://manati.star.nesdis.noaa.gov/datasets/>.
- [10] T. W. Gerling. Structure of the surface wind field from the seasat sar. *J. Geophys. Res.*, 91(C2):2308–2320, 1986.
- [11] F. Girard-Ardhuin, G. Mercer, and R. Garello. Oil slick detection by SAR imagery: potential and limitations. In *OCEANS*, 2003.
- [12] K. Hasselmann and S. Hasselmann. On the nonlinear mapping of an ocean wave spectrum into a synthetic aperture radar image spectrum and its inversion. *Journal of Geophysical Research*, 96(C6):10713–10729, June 1991.
- [13] Jochen Horstmann and Wolfgang Koch. Measurement of ocean surface winds using synthetic aperture radars. *Oceanic Engineering, IEEE Journal of*, 30(3):508–515, 2005.
- [14] Koninklijk Nederlands Meteorologisch Instituut. <http://www.knmi.nl/scatterometer/>.
- [15] B. Kinsman. *Wind waves: their generation and propagation on the ocean surface*. Prentice-Hall, 1965.
- [16] Haiyan Li, William Perrie, Lanli Guo, and Biao Zhang. On polarimetric characteristics in sar images of mesoscale cellular convection in the marine atmospheric boundary layer. *Journal of Geophysical Research. Oceans*, 116(8), 2011.
- [17] Y. Liu, X. Yan, and M.-Y. Su. Directional spectrum of wind waves: Part I – model and derivation. *Journal of Ocean University of Qingdao*, 2(1):1–12, April 2013.
- [18] NASA/JPL. Winds: Missions. <http://winds.jpl.nasa.gov/missions/index.cfm>.
- [19] NOAA. Monthly/seasonal climate composites. <http://www.esrl.noaa.gov/psd/cgi-bin/data/composites/printpage.pl>.
- [20] NOAA. National data buoy center. <http://www.ndbc.noaa.gov/>.
- [21] C. Oliver and S. Quegan. *Understanding Synthetic Aperture Radar Images*. SciTech, 2004.
- [22] M. Rey. Application of Radon transform techniques to a wake detection in SEASAT. *IEEE Geosciences and Remote Sensing*, 1990.
- [23] M. Robinson. Understanding networks and their behaviors using sheaf theory. In *IEEE Global Conference on Signal and Information Processing (GlobalSIP)*, Austin, Texas, 2013.
- [24] A. Stoffelen. A simple method for calibration of a scatterometer over the ocean. *Journal of Atmospheric and Oceanic Technology*, 16, 1999.
- [25] S. Strogatz. *Nonlinear Dynamics And Chaos*. Perseus, 2008.
- [26] Weather Underground. Weather history for Christmas Island, Monday, November 26, 2012. <http://www.wunderground.com/history/airport/YPXM/2012/11/26/DailyHistory.html>.
- [27] I. R. Young and W. Rosenthal. A three-dimensional analysis of marine radar images for the determination of ocean wave directionality and surface currents. *Journal of Geophysical Research*, 90(C1):1049–1059, January 1985.

DEPARTMENT OF MATHEMATICS AND STATISTICS, AMERICAN UNIVERSITY, 4400 MASSACHUSETTS AVE NW, WASHINGTON, DC 20016

*E-mail address:* [michaelr@american.edu](mailto:michaelr@american.edu)